

Identification of Ground Targets From Sequential High-Range-Resolution Radar Signatures

XUEJUN LIAO

PAUL RUNKLE

LAWRENCE CARIN, Fellow, IEEE
Duke University

An approach to identifying targets from sequential high-range-resolution (HRR) radar signatures is presented. In particular, a hidden Markov model (HMM) is employed to characterize the sequential information contained in multiaspect HRR target signatures. Features from each of the HRR waveforms are extracted via the RELAX algorithm. The statistical models used for the HMM states are formulated for application to RELAX features, and the expectation-maximization (EM) training algorithm is augmented appropriately. Example classification results are presented for the ten-target MSTAR data set.

Manuscript received April 11, 2001; revised October 15, 2001 and March 25 and April 10, 2002; released for publication May 9, 2002.

IEEE Log No. T-AES/38/4/06544.

Refereeing of this contribution was handled by E. S. Chornoboy.

Authors' current addresses: X. Liao and L. Carin, Dept. of Electrical and Computer Engineering, Duke University, PO Box 90291, Durham, NC 27708-0291; P. Runkle, Microelectronics Center of North Carolina, Purham, NC 27709.

0018-9251/02/\$17.00 © 2002 IEEE

I. INTRODUCTION

There are many applications for which one is interested in performing target detection and classification based on a sequence of high-range resolution (HRR) radar signals [1–7]. In such scenarios one implicitly views the target from a sequence of observations, due to target and/or sensor motion. One approach to processing such a sequence of waveforms is to form a synthetic aperture radar (SAR) or inverse SAR (ISAR) image [5, 6, 8, 18, 19] with subsequent detection/classification performed in the image domain. We consider an alternative approach, in which one processes the sequence of HRR waveforms directly, without explicitly forming an image. Since SAR/ISAR are preferable for the case of fixed targets, the technique presented here is most appropriate for moving targets. The sequence of waveforms is processed using a hidden Markov model (HMM), HMMs having been utilized previously for processing data from several sequential-scattering problems [9–11]. The principal contributions of this paper involve development of techniques for characterization of the HMM states, for the case of HRR data. Moreover, algorithm performance is examined using the MSTAR data set [17]. Below we review the HMM paradigm, as applied to multiaspect scattering data, and discuss issues associated with its application to HRR data.

Before proceeding, however, it is important to emphasize that the approach presented here is most appropriate for the case of moving targets, since the two-dimensional imagery afforded by SAR is generally preferable when the target is fixed. The connection between joint sensing of moving and stationary targets has been discussed in [20]. For the case of moving targets one will often have a good a priori estimate of the target pose (e.g. from Doppler information), while this is clearly unavailable for the case of a fixed target. We note that in the example results discussed in Section IV, we consider fixed targets from the MSTAR data set. This is simply based on the availability of data, rather than a specific endorsement of HRR for fixed (stationary) targets.

HRR scattering from complex targets yields target signatures that are a strong function of the target-sensor orientation [1–7]. Nevertheless, there are generally contiguous sets of orientations (aspects) for which the scattering physics vary slowly, and for which the associated HRR waveforms can be approximated as stationary statistically. Each such set of angles is termed a “state” [9–11]. When one measures multiple HRR waveforms from a sequence of target-sensor orientations, one implicitly samples waveforms from a sequence of target states. Since the targets of interest are distant and possibly concealed, both the target identity and pose are unknown, and therefore the particular set of states that are

sampled is deemed “hidden.” In many applications the sequence of sampled states can be characterized via a Markov process, the overall construct therefore yielding an HMM. This basic paradigm has been applied to several scattering problems [9–11], with characterization of the state-dependent statistics constituting the most problem-dependent HMM component. We extend characterization of the state-dependent statistics to the case of HRR data.

There has been much previous work on characterizing HRR statistics for individual waveforms [1–4, 7], with this extended here to the multispect case. Some authors have developed models for the statistics of the HRR range bins, without performing feature extraction [4, 12]. In this approach one typically must make assumptions concerning the range-bin-dependent statistics. For example, the constrained quadratic classifier [4, 12] is based on an uncorrelated-Gaussian model for the range-bin amplitudes. Alternatively, one can perform feature extraction, with this often manifesting dimensionality reduction. Recent HRR studies have considered “peak-amplitude features” [4]. Other example feature extractors include the RELAX algorithm [13], from which waveform constituents are extracted, these characteristic of the principal target scattering centers. We consider RELAX feature extraction, and develop two distinct statistical models. The key novelty of these statistical models, *vis-à-vis* previous studies [1–4, 7], is that the aforementioned HRR models are used as components in an HMM. In particular, a distinct statistical model is used for each state of the HMM, recalling that an HMM state is characterized by a set of target-sensor orientations over which the associated scattered waveforms are approximately stationary. The statistical relationships between a sequence of HRR waveforms are accounted for via the HMM probabilities of transitioning from one state to the next, for a given angular sampling rate [9–11].

The remainder of the text is organized as follows. In Section II we briefly review the HMM construct, followed by a detailed discussion on how the state-dependent HRR statistics are characterized and employed in the context of the HMM states. The MSTAR data set is reviewed in Section III, along with a discussion of how such is used to generate a sequence of HRR waveforms. Several sets of example results are presented in Section IV, with conclusions summarized in Section V.

II. HMM PROCESSING OF SEQUENTIAL HRR DATA

A. HMM Basics

Fig. 1 represents a typical configuration for airborne interrogation of a ground target. The airborne radar periodically transmits coherent pulses of microwave energy, which impinge the

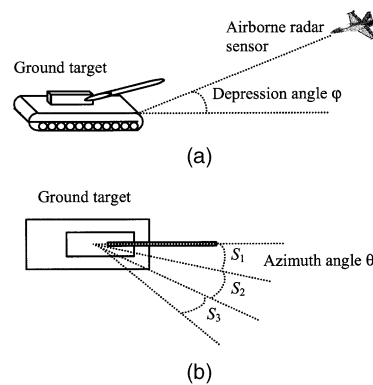


Fig. 1. Schematization of how the HMM is used to process a sequence of HRR waveforms. (a) Target is viewed from constant depression angle and multiple azimuthal positions. (b) Azimuthal variation of scattered fields characterized by set of states (here three shown), over which scattering physics approximately stationary.

ground target at depression angle φ . Each pulse is subsequently reflected from the target and received by the radar. After some preprocessing of these scattered radar echo pulses, a sequence of HRR signatures is obtained, each representative of the target as viewed from a distinct target-sensor orientation (with particular target-sensor orientations dependent on the sensor motion and target pose, with the latter typically unknown). For simplicity, in the studies presented here the depression angle is assumed constant, and therefore the variable target-sensor orientations are modeled as a change in the azimuthal orientation. The depression angle of the incident wave can be maintained as constant by controlling the sensor flight path, although in practice this constant-depression-angle assumption may have to be relaxed.

It is well known that HRR signatures exhibit significant variability as viewed from different orientations [1–4, 7]. Nevertheless, there are typically contiguous angular sectors over which the scattered fields are approximately stationary statistically. As discussed in the Introduction, each such sector is termed a “state,” and the sequence of HRR measurements sample waveforms from a sequence of target states, with this sequence well characterized via a Markov model [9–11]. In practice the target orientation is unknown (or “hidden”), in addition to the target identity, and therefore the sequence of scattered waveforms is characterized by an HMM.

In the classification algorithm an HMM is designed for each target of interest. A given set of sequential HRR data under test is submitted to all HMMs, and the data is associated with that target for which the respective HMM yields the largest likelihood. If the likelihoods from all HMM classifiers are below a prescribed threshold, then the sequential data can be declared not representative of any of the targets seen while training.

Assume a target is partitioned into N distinct states, denoted by the set $S = \{s_1, s_2, \dots, s_N\}$. As discussed above, here the states constitute an azimuthal partitioning. The HMM state-transition probabilities are denoted by the matrix $\mathbf{A} = \{a_{ij}\}$, where a_{ij} is the probability of transiting on consecutive measurements from state i to state j . Further, the initial-state probabilities are denoted by the vector $\pi = \{\pi_i\}$, where π_i is the probability of sampling state i on the first measurement (of the sequence). For the sequence of HRR measurements, assume that $\delta\theta$ represents the change in the target-sensor orientation, upon consecutive measurements. Let θ_i represent the angular extent of state i . We assume $\delta\theta < \theta_i$, for all i , implying that on consecutive measurements one can stay in the same state or transition into an adjacent state. This yields a tri-diagonal state-transition matrix \mathbf{A} . Based on the aforementioned assumptions with regard to $\delta\theta$ and θ_i , one can readily demonstrate the following estimations for the state-transition probabilities:

$$a_{i,i-1} = a_{i,i+1} = \delta\theta/(2\theta_i) \quad a_{i,i} = (\theta_i - \delta\theta)/\theta_i. \quad (1)$$

Moreover, if the initial target pose is uniformly distributed azimuthally, we similarly have

$$\pi_i = \frac{\theta_i}{\sum_{i=1}^N \theta_i}. \quad (2)$$

As discussed further below, (1) and (2) constitute initial estimates for \mathbf{A} and π , with these refined via Baum–Welch training [14] (see Section IIC).

B. State-Dependent Statistics: RELAX

Consider the frequency-dependent complex HRR waveform $X(\omega)$, scattered from a given target at a particular (generally unknown) target-sensor orientation. The RELAX algorithm [13] is used to extract point-scattered wavefronts from $X(\omega)$, from which the range (time) dependent HRR waveform is realized

$$x(r) = \sum_{k=1}^K A_k^x w(r - r_k^x) \quad (3)$$

where $x(r)$ is the Fourier transform of an approximation to $X(\omega)$, with $X(\omega)$ approximated from the K wavefronts extracted from RELAX. Each RELAX-extracted wavefront is representative of a point scatterer, with $A_k^x = a_k^x \exp(j\phi_k^x)$ constituting the complex amplitude of the k th wavefront (magnitude a_k^x), and $w(r)$ is the real window function used to represent the spatial support of the wavefronts (defined by system bandwidth). The symbol r_k^x represents the time of arrival of the k th wavefront, extracted via RELAX. In the work presented here $w(r)$ is a Gaussian with variance consistent with the sensor bandwidth. For each complex HRR waveform (3) we

define the real and positive function

$$\tilde{x}(r) = \sum_{k=1}^K a_k^x w(r - r_k^x). \quad (4)$$

Now consider two HRR signatures $\tilde{x}(r)$ and $\tilde{y}(r)$, for which we wish a distance measure. The distance is defined in terms of the correlation

$$\begin{aligned} C(x, y) &= \int dr \tilde{x}(r) \tilde{y}(r) = \sum_{k=1}^K \sum_{i=1}^K a_k^x a_i^y \\ &\quad \times \int w(r - r_k^x) w(r - r_i^y) dr \\ &= \sum_{k=1}^K \sum_{i=1}^K a_k^x a_i^y g(r_k^x - r_i^y). \end{aligned} \quad (5)$$

Since $w(r)$ is Gaussian, so is $g(r)$, with twice the variance. Using matrix notation, (5) can be rewritten as

$$C(x, y) = \mathbf{a}_x^T \mathbf{W}_{xy} \mathbf{a}_y \quad (6)$$

with \mathbf{W}_{xy} a $K \times K$ matrix representing the functions $g(r_k^x - r_i^y)$. Superscript T represents transpose of a column vector. Note that the correlation in (5) can be computed directly from the RELAX outputs, without having to explicitly form the range profile (4).

We now define the distance

$$d^2(x, y) = \mathbf{a}_x^T \mathbf{W}_{xx} \mathbf{a}_x + \mathbf{a}_y^T \mathbf{W}_{yy} \mathbf{a}_y - 2\mathbf{a}_x^T \mathbf{W}_{xy} \mathbf{a}_y \quad (7)$$

which is referred to as the spatially weighted distance (SWD), in which each element in the weighting matrix is a function of spatial distance between scatterers. In (7) \mathbf{W}_{xx} and \mathbf{W}_{yy} are of the same form as \mathbf{W}_{xy} . Note that if the wavefronts are spaced uniformly, such that $\Delta = r_{k+1}^x - r_k^x = r_{i+1}^y - r_i^y$ and $g(\Delta) = 0$, then this distance measure reduces to the traditional Euclidean distance

$$d^2(x, y) = \mathbf{a}_x^T \mathbf{a}_x + \mathbf{a}_y^T \mathbf{a}_y - 2\mathbf{a}_x^T \mathbf{a}_y = (\mathbf{a}_x - \mathbf{a}_y)^T (\mathbf{a}_x - \mathbf{a}_y). \quad (8)$$

The distance measure in (7) plays a pivotal role in the HRR HMM, as currently designed. In particular, for the N states $S = \{s_1, s_2, \dots, s_N\}$ characteristic of a given target, we define a codebook of N codes $C = \{c_1, c_2, \dots, c_N\}$, with code c_n associated with state s_n . Recall that the HMM requires a state-dependent statistical measure. In the context of RELAX feature extraction, we have implemented this in two ways.

Consider a sequence of M HRR waveforms, representative of viewing the target from a sequence of M orientations, with each waveform parsed into a set of K point-scatter features via RELAX. In the context of a discrete HMM [11], each set of RELAX features is mapped into a distinct codebook element (a code from C), using a nearest neighbor mapping implemented via the distance measure in (7). In this context each HRR waveform in

the sequence of M is mapped to a distinct code (analogous to vector quantization [15]), and therefore after quantization the original M HRR waveforms are represented by a sequence of M codes (each a member of C). The HMM is used to define the target for which such a sequence of codes is most likely. The state-dependent probability of observing a particular code is characterized via a matrix $\mathbf{B} = \{b_{ij}\}$ where b_{ij} represents the probability of observing code i in state j .

While a discrete HMM is relatively simple, being characterized by the set of codes C , state-transition matrix \mathbf{A} , initial-state probabilities π , and the state-dependent probability matrix \mathbf{B} , such a model has well-known limitations. In particular, there is distortion [15] when one performs the aforementioned vector quantization, thus undermining performance. Moreover, as the number of targets of interests increases, the number of codes also increases, making \mathbf{B} a large matrix (this issue is discussed further below).

To mitigate these problems, we have also considered a continuous HMM [14]. We again define a codebook $C = \{c_1, c_2, \dots, c_N\}$, with code c_n associated with state s_n . For a given HRR signal x the likelihood that x is associated with state s_n is defined as

$$p(x | s_n) = \frac{1}{\sqrt{2\pi}\eta_n} \exp\left[-\frac{d^2(x, c_n)}{2\eta_n^2}\right]. \quad (9)$$

The likelihood in (9) is clearly motivated by a Gaussian distribution, but here we explicitly utilize the distance measure d^2 , which is tied to the RELAX features extracted from the HRR waveform. Therefore, the continuous HMM is of the same form as its discrete counterpart, with the \mathbf{B} matrix in the latter replaced in the former by $p(x | s_n)$.

It is worthwhile to emphasize an important distinction between the continuous and discrete HMMs. As implemented here both methods employ a codebook C , but they utilize such in distinct ways. Considering first the discrete HMM, the HMM matrix \mathbf{B} associated with a given target must include the codes across all targets of interest. If, by contrast, the \mathbf{B} matrix associated with a given target T_i were only to use codes associated with T_i , then the quantization procedure for the associated HMM would map any HRR profile into a code characteristic of T_i . Therefore, in \mathbf{B} we utilize the complete set of codes for all targets of interest, accounting for target-dependent code diversity. Consequently the size of \mathbf{B} grows with the number of targets of interest. On the other hand, the density function $p(x | s_n)$ utilized in the continuous HMM accounts for waveforms that are not matched to a given target-dependent codebook by yielding a low likelihood (ideally, if x is not associated with state s_n , $p(x | s_n)$ will be small). Hence, in defining $p(x | s_n)$ for a given continuous HMM, one only employs

codes from the associated target, and therefore the continuous-HMM complexity does not increase with the number of targets.

Concerning the design of the state decomposition $S = \{s_1, s_2, \dots, s_N\}$ and the associated set of codes $C = \{c_1, c_2, \dots, c_N\}$, we initially divide the scattering data into N states, using a uniform angular decomposition (for N states, each has angular extent $360^\circ/N$). Using the training data associated with target T_i we perform RELAX on all HRR waveforms, and the code c_n is the average of the RELAX features from state s_n . The above state decomposition and codes only constitute an initialization, with this optimized subsequently via the expectation-maximization (EM) algorithm discussed in Section IIC.

C. Expectation-Maximization HMM Optimization

The discussions in Section IIB employed state-dependent statistical models based on an assumed state decomposition. Moreover, various averaging procedures have been employed to compute such HMM components as codebooks (discrete HMM) and density-function parameters (continuous HMM), once the state decomposition is defined. Clearly the quality of the associated HMM is dictated by the quality of such model-parameter estimations. We have therefore employed optimization algorithms to refine the HMM parameters, and therefore the model-parameter computations discussed in Section IIB are simply initializations for the model parameters, followed by the optimization procedure discussed below.

The EM HMM training algorithm starts by defining the forward variable

$$\alpha_m(n) = p(o_1 o_2 \dots o_m, q_m = s_n | \lambda) \quad (10)$$

and backward variable

$$\beta_m(n) = p(o_{m+1} o_{m+2} \dots o_M | q_m = s_n, \lambda) \quad (11)$$

where $O = \{o_1, o_2, \dots, o_M\}$ is representative of the sequence of M observed HRR waveforms (more specifically, the components of the M HRR profiles used in the HMM model), q_m is the state sampled by the m th measurement (this "hidden"), s_n represents the n th state of a given target (with $n = 1, 2, \dots, N$), and λ represents the associated HMM parameters. We define two intermediate variables

$$\begin{aligned} \xi_m(i, j) &= p(q_m = s_i, q_{m+1} = s_j | O, \lambda) \\ &= \frac{p(O, q_m = s_i, q_{m+1} = s_j | \lambda)}{p(O | \lambda)} \\ &= \frac{\alpha_m(i) a_{ij} b_j(o_{m+1}) \beta_{m+1}(j)}{\sum_{i=1}^N \sum_{j=1}^N \alpha_m(i) a_{ij} b_j(o_{m+1}) \beta_{m+1}(j)} \end{aligned} \quad (12)$$

and

$$\begin{aligned}\gamma_m(i) &= p(q_m = s_i | O, \lambda) \\ &= \frac{p(O, q_m = s_i | \lambda)}{p(O | \lambda)} \\ &= \frac{\alpha_m(i)\beta_m(i)}{\sum_{i=1}^N \alpha_m(i)\beta_m(i)} = \sum_{j=1}^N \xi_m(i, j).\end{aligned}\quad (13)$$

In (12) the expression $b_j(O_{m+1})$ represents the likelihood of observing O_{m+1} in state j . For the discrete HMM, O_{m+1} corresponds to a discrete code (after quantization), while for a continuous HMM it corresponds to RELAX features (Section IIB). In particular, for the continuous HMM employing RELAX features $b_j(O_{m+1})$ is represented by (9).

Given the observation sequence $O = \{o_1, o_2, \dots, o_M\}$ and the current HMM parameters λ , the Baum–Welch algorithm reestimates the HMM parameters as

$$\hat{\pi}_i = \gamma_1(i) \quad (14)$$

$$\hat{a}_{ij} = \frac{\sum_{m=1}^{M-1} \xi_m(i, j)}{\sum_{m=1}^{M-1} \sum_{j=1}^N \xi_m(i, j)}. \quad (15)$$

and the code associated with state n is approximated as

$$\hat{c}_n = \frac{\sum_{m=1}^M \gamma_m(n) \cdot o_m}{\sum_{m=1}^M \gamma_m(n)}. \quad (16)$$

For the case of the continuous HMM, based on RELAX features, the EM update procedure is more involved. The associated details are summarized in Appendix A.

The EM algorithm iterates by using the new HMM parameters λ reflected in (14)–(16) to recompute the parameters in (10)–(13), with this process repeated until λ converges. Upon convergence the match between the training data (represented by the training observation sequences O) and HMM models is improved, generally increasing the likelihood of the training data when applied to the final HMM (relative to the HMM using the original model parameters). However, we note that the EM algorithm does not in general yield the global optimal maximum likelihood (ML) solution, and therefore a good initialization is important. We here utilize the initialization discussed in Sections IIA and IIB.

A final point is in order concerning the HMM training. The EM algorithm is designed to maximize the likelihood of a given set of training data, as applied to the associated HMM statistical model. When training a given HMM, we therefore utilize no additional information concerning other targets that may be encountered. If desired, one could design the HMM for target T_i such that the likelihood of the training data is maximized when submitted to the associated model, while simultaneously minimizing

the likelihood for training data associated with all other known targets $T_j \neq T_i$. This approach may yield improved classification performance, but it assumes knowledge of other targets that may be encountered. We have not utilized this HMM-design approach, although in some applications it may be appropriate.

III. DATA SET UNDER CONSIDERATION

We consider the MSTAR data set for testing the algorithms discussed in Section II. As elucidated in other papers [5, 6], the MSTAR data consists of X-band scattering from ten targets. The data typically consists of image chips. These images have been converted into a sequence of HRR waveforms, through several filtering operations. The HRR data was provided to the investigators by the US Defense Advanced Research Projects Agency (DARPA), with the conversion of MSTAR images to HRR waveforms performed under the DARPA TRUMPETS program. All ground-based targets are of very similar shape (most are military vehicles, although there are a few civilian vehicles [5, 6]).

We provide a brief summary of how MSTAR images are converted to aspect-dependent HRR signatures (for more details, see [17]). Consider an MSTAR image $i(z, y)$, where z reflects the downrange dimension and y the cross range. The image consists of bipolar real pixel values. A two-dimensional (2-D) inverse fast Fourier transform (FFT) is first taken of $i(z, y)$ to obtain the associated phase-history data. The original images are weighted and over-sampled, so the phase history is a convolved and zero-padded version. We next perform deconvolution of the weighting and removal of the zero-padding, followed by a 2-D FFT, to produce a deconvolved and Nyquist-sampled image $\tilde{i}(z, y)$ that contains both the target and any surrounding clutter. We now extract that portion of the resulting image associated with the target of interest (segmentation). An inverse FFT is now performed in the y dimension, for all z , from which each z -dependent waveform, for a fixed y , corresponds to an HRR profile. Using multiple images $i(z, y)$ for a given target, corresponding to distinct rotational positions of the target relative to the sensor aperture, we extract HRR profiles from numerous target-sensor orientations. The multiple aspect-dependent HRR profiles for a given target type and depression are then placed into contiguous 1° azimuthal bins. The sponsor segregated the data into distinct training and testing sets. As discussed below, the size of the training and testing data was set to be equal. This segmentation of testing and training data was specified by DARPA under the TRUMPETS program. The HRR signatures have a bandwidth of 600 MHz centered at 10 GHz, and have a range resolution of approximately 0.3 m.

The data is considered at two depression angles (15° and 17°), and for each the variable azimuthal

positions are distributed in the full range of 360° , with azimuthal sampling approximately 0.1° as discussed above. As described in Section IIA, our HMM model is valid for any angular sampling rate $\delta\theta$ that satisfies $\delta\theta < \min_i(\theta_i)$, where θ_i is the angular extent of the i th HMM state. With the 0.1° rate each target is characterized by 3,601 HRR waveforms over the full 360° aspect range, resulting in a cumulative total of 36,010 training signatures and 36,010 testing signatures for the ten targets. The testing and training data is distinct, as defined by the aforementioned random partitioning. Due to the uniform azimuth sampling, an equal number of training and testing waveforms are obtained. The depression angle (relative to grazing) is 15° for all examples considered.

IV. EXAMPLE RESULTS

A. Preliminaries

In the first set of example results, we consider a 3° angular aperture for the sequential HRR data under test, which at the angular sampling rate of $\delta\theta = 0.1^\circ$ corresponds to a sequence of $M = 31$ scattered waveforms. Each of the ten MSTAR targets under consideration is partitioned into 120 states, over a 360° azimuthal angular range, corresponding to an initialization of 3° state sizes (this is reapportioned in the HMM training, so that the state sizes subsequently adjust to account for the scattering physics). The large number of states is reflective of the target complexity (as described further below) and the small operating wavelength (3 cm) relative to characteristic target dimensions.

In Section IIIA we discussed a discrete HMM, in which the features associated with each HRR waveform are mapped to a code, and therefore the sequence of M HRR profiles is transformed to a sequence of M codes. We have implemented such an HMM in the context of RELAX feature parsing (the codes represent a discretization of the RELAX feature space). We have found that, for the MSTAR data set, the discrete HMM yields performance worse than that of a continuous HMM, and therefore all results reported here are for continuous HMMs. The discrete HMM is also undesirable due to the very large \mathbf{B} matrix characteristic of the ten targets under test (see Section IIB).

One of the significant complicating issues in multiaspect HRR scattering is the scintillation caused by relatively small scattering centers that come in and out of view with relatively small changes in aspect (target-sensor orientation). By limiting RELAX wavefront extraction to the relatively large scatterers, we mitigate scintillation to some extent. In the course of the work reported here, we have extracted the $K = 15$ principal wavefronts (scattering centers) from

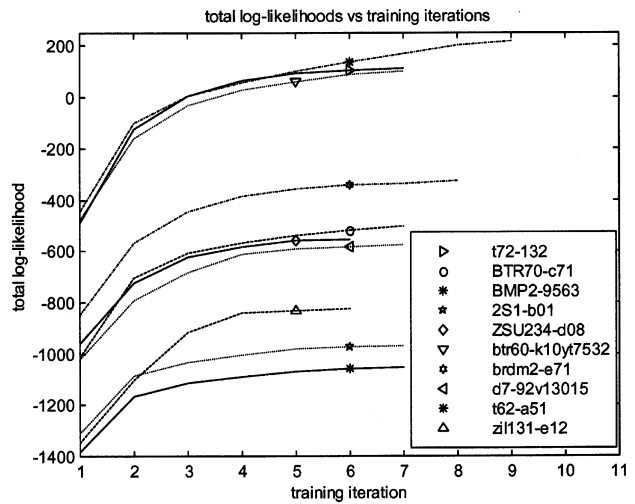


Fig. 2. Total likelihood as function of EM-algorithm iteration number. Results shown for extended Baum–Welch training with one long forward sequence and one backward sequence covering clockwise and counterclockwise directions in full 360° azimuthal range and with 0.1° azimuth sampling. Fixed 15° depression used.

each of the $M = 31$ scattered waveforms in the 3° angular sequence. For these studies the parameter K has not been optimized. Such optimization is a subject of significant interest, in that K should be small enough to avoid relatively small scattering centers that may lead to scintillation, while being large enough to extract the principal scattering centers robustly and retain sufficient information to aid classification performance.

B. HMM Training

There are many methods for selecting the training sequences. Here we train the HMM from a long forward sequence and a long backward sequence. A long forward sequence is the sequence of waveforms with azimuths in the forward order $0^\circ \rightarrow 0.1^\circ \rightarrow \dots \rightarrow 359.9^\circ \rightarrow 360^\circ$ while a long backward sequence are the same waveforms but with azimuths in reversed order. These sequences capture all sequential information and state statistics. The only information left out is the initial state probability distribution π . However we can easily account for this via geometry, as implemented in (2). We train a HMM using the training sequences from each of the ten MSTAR targets and thus obtain ten distinct HMM models. To show the convergence of the EM algorithm, in Fig. 2 we plot for each HMM model the total likelihood as a function of the EM training iteration number. It is seen that the likelihood exhibits a monotonic increase over iterations as expected by the EM algorithm. The likelihood converges after 6–9 iterations. This can be attributed to the good guess of the initial HMM parameters and the long-sequence selection scheme.

The EM training can be viewed as an evolution of the state decomposition, that is, as the training

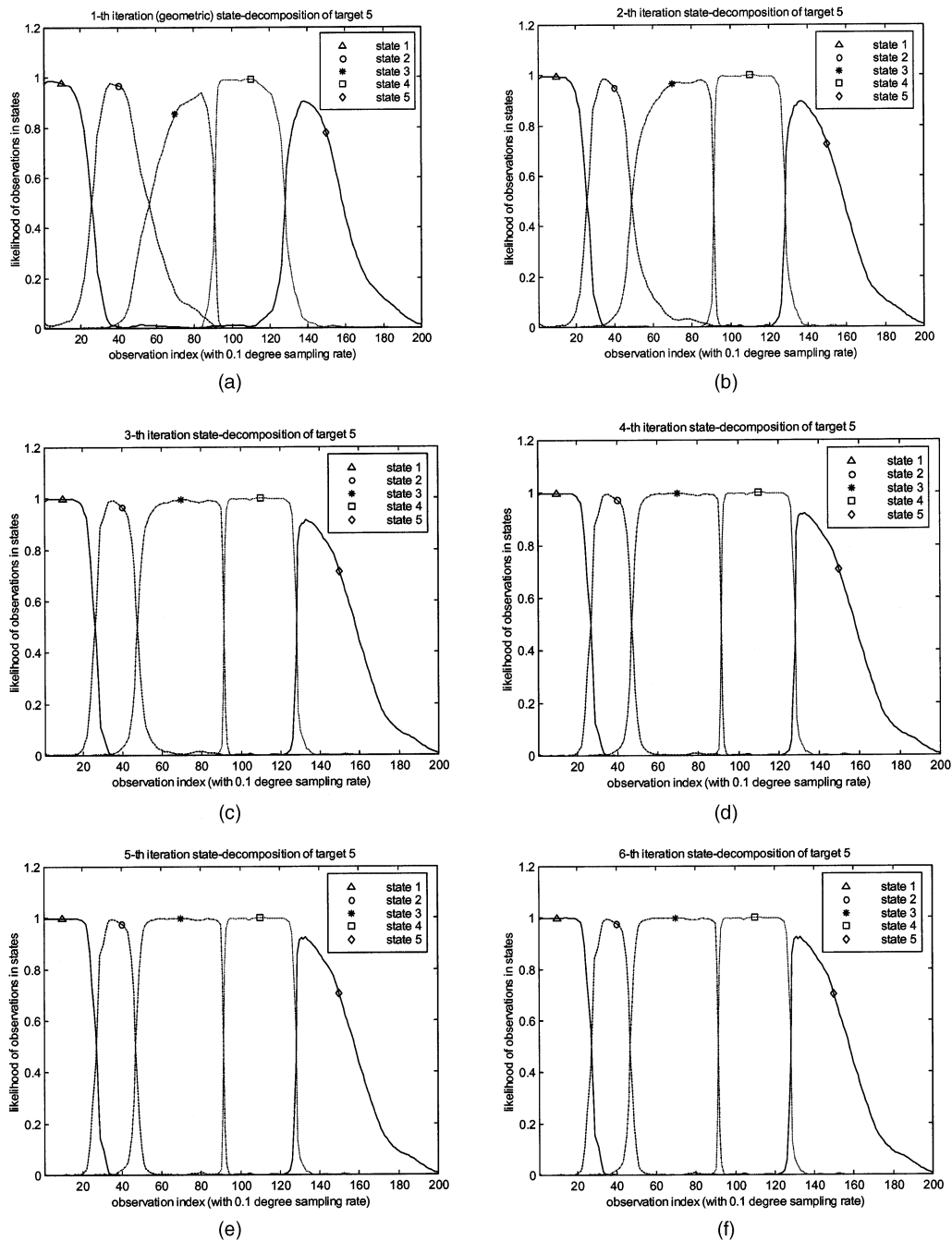



Fig. 3. Convergence of state decomposition as function of EM-algorithm iteration number. Results shown for 20° deg of sequential data, 0.1° angular sampling. Data corresponds to ZSU target (see Table I). (a) Iteration one. (b) Iteration two. (c) Iteration three. (d) Iteration four. (e) Iteration five. (f) Iteration six.

proceeds, each state has more clearly defined boundaries. To demonstrate this, we consider a sequence of 200 HRR profiles from target ZSU234, over a 20° angular extent (recall the 0.1° sampling). We plot in Fig. 3 the likelihood that each of the 200 profiles is associated with a given HMM state, with the states considered encompassing the range of angles under consideration (here we consider five states). To be specific, for each iteration of the EM algorithm, we compute the likelihood that the m th measurement in the sequence (the m th

HRR waveform) is associated with state s_i . This is quantified using $\gamma_m(i)$ from (13). Note that initially the states are defined by a uniform decomposition in azimuth, and each is 3° in extent (the initialization described in Section II). As the EM algorithm iterates, the state partitioning is adjusted, such that the states are no longer necessarily of the same angular extent. Moreover, upon convergence, the state decomposition and the associated parameters are such that each HRR profile is more clearly associated with a particular state. We see from Fig. 3 that the EM algorithm

TABLE I
Confusion Matrix for Ten MSTAR Targets



| | | HMM models of different targets | | | | | | | | | |
|--------------------------------|--------|---------------------------------|--------|--------|--------|--------|--------|--------|--------|--------|--------|
| | | T72 | BTR70 | BMP2 | 2S1 | ZSU234 | BTR60 | BRDM2 | D7 | T62 | ZIL131 |
| Test data of different targets | T72 | 84.122 | 0.336 | 1.484 | 1.596 | 2.072 | 0.728 | 2.268 | 4.509 | 0.196 | 2.688 |
| | BTR70 | 0.784 | 77.289 | 3.136 | 3.752 | 2.212 | 5.881 | 1.988 | 1.232 | 2.604 | 1.120 |
| | BMP2 | 3.668 | 1.596 | 79.782 | 3.976 | 4.705 | 0.952 | 0.336 | 1.792 | 0.392 | 2.800 |
| | 2S1 | 2.100 | 2.436 | 3.360 | 81.994 | 2.632 | 1.736 | 1.456 | 1.232 | 1.680 | 1.372 |
| | ZSU234 | 1.120 | 0.840 | 3.080 | 1.624 | 84.262 | 0.672 | 0.924 | 2.492 | 3.472 | 1.512 |
| | BTR60 | 0.644 | 1.456 | 0.952 | 1.932 | 7.449 | 78.885 | 1.988 | 1.960 | 3.164 | 1.568 |
| | BRDM2 | 0.196 | 5.013 | 3.752 | 1.596 | 1.624 | 2.408 | 82.890 | 1.064 | 0.000 | 1.456 |
| | D7 | 1.932 | 1.568 | 0.924 | 1.008 | 1.512 | 1.232 | 1.260 | 88.715 | 1.428 | 0.420 |
| | T62 | 1.484 | 0.756 | 0.364 | 0.952 | 4.088 | 1.288 | 0.168 | 3.640 | 84.290 | 2.968 |
| | ZIL131 | 1.064 | 0.756 | 0.756 | 1.652 | 5.853 | 1.904 | 0.644 | 1.456 | 1.120 | 80.062 |
| Average rate | 82.229 | | | | | | | | | | |

Note: Classification rate (in percent) shown using 3° aperture and 0.1° azimuthal sampling (a sequence of 31 HRR waveforms). Photographs shown of each target.

TABLE II
Confusion Matrix for Ten MSTAR Targets

| | | HMM models of different targets | | | | | | | | | |
|--------------------------------|--------|---------------------------------|--------|--------|--------|--------|--------|--------|--------|--------|--------|
| | | T72 | BTR70 | BMP2 | 2S1 | ZSU234 | BTR60 | BRDM2 | D7 | T62 | ZIL131 |
| Test data of different targets | T72 | 91.895 | 0.480 | 0.085 | 0.875 | 2.881 | 0.706 | 1.243 | 1.186 | 0.000 | 0.650 |
| | BTR70 | 0.706 | 87.800 | 2.231 | 1.327 | 1.214 | 3.050 | 1.327 | 0.000 | 2.146 | 0.198 |
| | BMP2 | 2.739 | 0.593 | 91.782 | 1.243 | 0.988 | 0.085 | 0.000 | 0.875 | 0.198 | 1.497 |
| | 2S1 | 0.593 | 1.666 | 0.508 | 93.279 | 1.186 | 0.056 | 1.497 | 0.000 | 0.339 | 0.875 |
| | ZSU234 | 0.480 | 0.254 | 2.203 | 1.073 | 92.516 | 0.000 | 0.282 | 0.960 | 1.327 | 0.904 |
| | BTR60 | 0.508 | 0.395 | 0.141 | 1.864 | 4.886 | 86.416 | 0.706 | 0.904 | 3.022 | 1.158 |
| | BRDM2 | 0.113 | 2.400 | 1.469 | 1.186 | 0.085 | 0.311 | 93.646 | 0.000 | 0.000 | 0.791 |
| | D7 | 0.000 | 0.226 | 0.113 | 0.000 | 0.169 | 0.056 | 1.045 | 97.628 | 0.621 | 0.141 |
| | T62 | 0.000 | 0.000 | 0.847 | 0.480 | 2.287 | 0.000 | 0.000 | 0.480 | 95.369 | 0.537 |
| | ZIL131 | 0.960 | 0.000 | 2.429 | 0.311 | 2.175 | 1.892 | 0.904 | 0.085 | 0.000 | 91.245 |
| Average rate | 92.158 | | | | | | | | | | |

Note: Classification rate (in percent) shown using 6° aperture and 0.1° azimuthal sampling (a sequence of 61 HRR waveforms).

converges after five iterations for ZSU234 and that the final state decomposition is different from the initialization. We reiterate that the state decomposition is dictated by the scattering physics, with each state representative of approximately stationary scattering (as a function of target-sensor orientation).

C. HMM Classification

In Table I we present confusion-matrix results for the ten-target problem, considering all 3° sequences for all targets. Also shown in Table 1 are photographs of the ten (similar) targets under consideration. For the 3° angular data considered, we find that the RELAX-based HMM yields an average classification rate of 82%. In the RELAX algorithm there is no waveform averaging, with scintillation addressed by limiting the number of scattering centers extracted (here $K = 15$ in (3)). We have also tried using other

values of K , but for the data considered the results are similar. In fact, when K increases to $K = 20$, performance actually declines, presumably due to enhanced scintillation (inclusion of five additional scattering centers, the characteristics of which change quickly with variable target-sensor orientation).

Note that with 120 states per target, each state initialized at 3° in extent (with this adjusted during training, see Section IVB), a test sequence of 3° extent is likely to only realize a single state transition. Multiple targets may have similar states, but the character of multiple adjacent states is likely to be more target dependent. Therefore, by increasing the angular extent of the test sequence, the additional state transitions are likely to improve classification. In Table II we reconsider the RELAX-based HMM, but now consider sequences of 6° angular extent ($M = 61$, with 0.1° angular sampling). We see in

Table II that classification performance now improves considerably, to an average of 92%. Note that the same HMMs applied to the 3° sequences are applied directly for the 6° sequences. This underscores the HMM utility, since separate models are *not* required for different sequence lengths (image-based classifiers are dependent on the aperture size used for image formation).

D. Receiver Operating Curves

The results in Tables I and II considered classifying all ten targets at once, with a given sequence of scattered waveforms under test submitted to the HMMs from all ten targets. The data was classified as associated with that target for which the corresponding HMM yielded the largest likelihood. It is also of interest to consider the binary hypothesis test, for which one must choose between one of two events. In this case we assume that the data under test is representative of one of two hypotheses, where for our problem a given hypothesis is associated with a particular target. If HMM_1 is associated with hypothesis one, and HMM_2 associated with hypothesis two, we form the likelihood ratio $R = HMM_1/HMM_2$. A given sequence of scattered waveforms is submitted to HMM_1 and HMM_2 , from which R is computed. For a prescribed threshold t the data is associated with target one if $R > t$, and otherwise it is associated with target two. By varying the threshold t , we generate the probability of detection versus the probability of false alarm, termed the receiver operating characteristic (ROC).

In Figs. 4 and 5 we plot ROCs for the case in which one target is D7 (hypothesis one), and we consider each of the other nine targets individually as hypothesis two. This yields nine ROC curves. In Fig. 4 we consider a sequence length corresponding to a 3° aperture (as in Table I), while in Fig. 5 we consider results for the case of a 6° aperture (as in Table II). We see in Figs. 4 and 5 that we obtain very good classification within the context of the binary test. A similar set of examples was considered in [18].

E. Consideration of Targets Not Seen While Training

In the examples discussed above the training and testing data were segregated, although all data was measured from the same particular target (for example, all the T72 data came from a single, particular example of a T72). There are often differences between particular realizations of the same military target, with such differences complicating target classification. For example, for the data considered here we had available scattering data from eleven realizations of the T72 tank, manifested by different realizations of the fuel tank, antenna, etc.

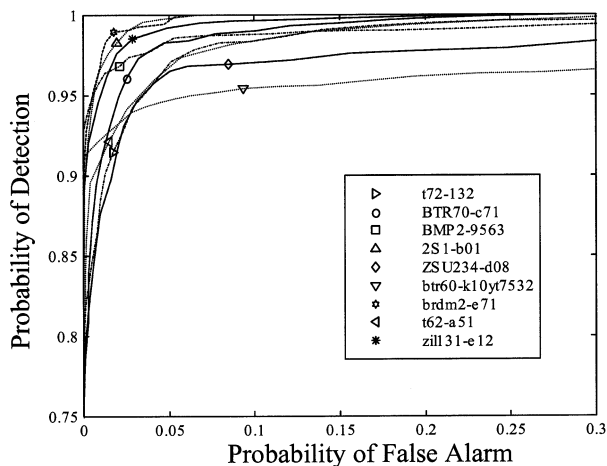


Fig. 4. ROC curves for target D7 as compared, one-by-one, with each of the other nine targets. Total aperture of 3° applied.

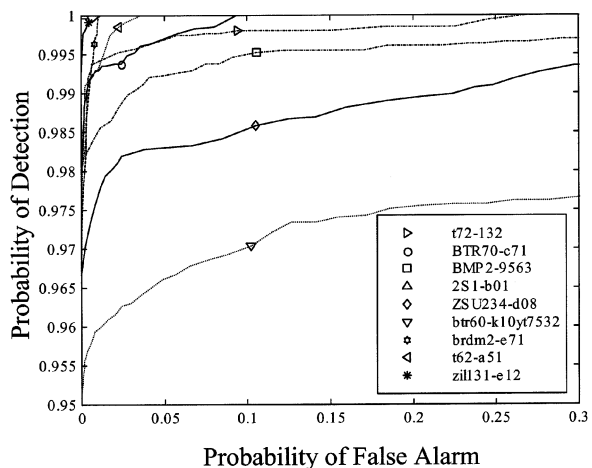


Fig. 5. ROC curves for target D7 as compared, one-by-one, with each of the other nine targets. Total aperture of 6° applied.

We also had three realizations of the BMP2 target. It is of significant interest to examine algorithm robustness to such differences in the particular target realization.

When one examines the scattered waveforms from different realizations of the T72 (for the eleven examples available), one often witnesses significant variation, for the same target-sensor position. This is reflective of the physical differences in the targets, as outlined above. We therefore performed the following test. We trained four distinct T72 HMM classifiers, using training data from four of the eleven available realizations of the target. The testing was then performed using data from all eleven realizations of the T72. The use of four classifiers for the same target was motivated by the desire to capture as large as possible a range in variation of the physical target realization. For the four T72 examples for which training data was used, the training and testing data were segregated in the manner discussed previously. With regard to the BMP2 target, we trained on two

TABLE III
Classification Results as in Table II, with Eleven Examples of T72 Target and Three Examples of BMP2 Target

| | T72_132 | t72_a04 | t72_a10 | t72_a62 | BTR70 | BMP2_9563 | bmp2_c21 | 2S1 | ZSU234 | BTR60 | BRDM2 | D7 | T62 | ZIL131 | total |
|-----------|---------|---------|---------|---------|-------|-----------|----------|------|--------|-------|-------|------|------|--------|-------|
| t72_132 | 85.3 | 1.7 | 2.4 | 3.0 | 0.7 | 0.1 | 1.1 | 1.1 | 1.3 | 0.5 | 1.0 | 1.5 | 0.0 | 0.4 | 92.4 |
| t72_812 | 18.8 | 25.2 | 7.5 | 18.9 | 2.5 | 1.7 | 0.6 | 0.7 | 5.2 | 2.1 | 0.0 | 0.7 | 3.0 | 13.1 | 70.4 |
| t72_s7 | 27.9 | 27.1 | 16.9 | 10.9 | 1.4 | 1.6 | 1.3 | 1.1 | 3.6 | 0.0 | 0.0 | 1.1 | 2.2 | 4.8 | 82.9 |
| t72_a04 | 0.0 | 92.0 | 2.7 | 2.5 | 0.0 | 0.0 | 0.0 | 0.0 | 0.5 | 0.0 | 0.0 | 2.1 | 0.0 | 0.3 | 97.1 |
| t72_a05 | 16.2 | 10.4 | 48.8 | 10.1 | 1.3 | 0.3 | 0.4 | 1.8 | 0.8 | 1.1 | 0.0 | 3.3 | 2.0 | 3.5 | 85.5 |
| t72_a07 | 10.5 | 14.2 | 42.6 | 16.7 | 2.5 | 3.4 | 0.2 | 0.9 | 1.9 | 1.6 | 0.3 | 3.7 | 0.7 | 0.9 | 83.9 |
| t72_a10 | 0.5 | 1.1 | 91.2 | 3.8 | 0.0 | 0.0 | 0.5 | 0.0 | 0.5 | 0.0 | 0.0 | 0.3 | 0.0 | 2.1 | 96.6 |
| t72_a32 | 9.0 | 37.1 | 19.1 | 11.9 | 0.0 | 3.0 | 3.1 | 3.4 | 1.6 | 0.3 | 0.0 | 2.3 | 2.0 | 7.2 | 77.1 |
| t72_a62 | 0.0 | 0.3 | 2.0 | 93.8 | 1.4 | 0.0 | 0.0 | 0.3 | 0.3 | 0.0 | 0.3 | 0.8 | 0.8 | 0.0 | 96.1 |
| t72_a63 | 1.0 | 26.2 | 13.6 | 43.3 | 0.0 | 0.0 | 0.2 | 0.0 | 1.3 | 0.4 | 0.5 | 5.7 | 6.7 | 1.2 | 84.1 |
| t72_a64 | 5.4 | 7.8 | 28.7 | 26.4 | 0.0 | 6.3 | 0.2 | 0.8 | 5.2 | 0.8 | 0.2 | 4.4 | 8.3 | 5.5 | 68.3 |
| BTR70 | 0.7 | 0.0 | 0.0 | 0.0 | 85.9 | 1.6 | 0.0 | 2.7 | 1.6 | 3.2 | 1.4 | 0.0 | 2.5 | 0.3 | 85.9 |
| bmp2_9563 | 1.8 | 0.3 | 0.4 | 0.0 | 0.7 | 84.0 | 9.0 | 0.7 | 1.0 | 0.1 | 0.0 | 0.4 | 0.0 | 1.6 | 93.0 |
| BMP2_9566 | 6.3 | 0.4 | 2.3 | 1.1 | 1.2 | 32.9 | 29.6 | 7.5 | 6.9 | 4.5 | 4.7 | 0.4 | 1.4 | 0.8 | 62.5 |
| BMP2_c21 | 1.1 | 0.5 | 0.5 | 0.0 | 0.3 | 3.5 | 90.4 | 0.4 | 1.5 | 0.0 | 0.1 | 0.0 | 0.0 | 1.8 | 93.9 |
| 2S1 | 0.6 | 0.2 | 0.0 | 0.0 | 1.4 | 0.1 | 0.6 | 95.3 | 0.5 | 0.0 | 0.4 | 0.0 | 0.2 | 0.6 | 95.3 |
| ZSU234 | 0.5 | 0.5 | 0.5 | 0.0 | 0.3 | 2.1 | 0.3 | 1.1 | 91.5 | 0.0 | 0.3 | 1.0 | 1.1 | 0.8 | 91.5 |
| BTR60 | 0.5 | 0.0 | 0.0 | 0.0 | 0.2 | 0.0 | 0.1 | 2.2 | 4.6 | 86.3 | 0.6 | 1.0 | 3.1 | 1.4 | 86.3 |
| BRDM2 | 0.1 | 0.0 | 0.0 | 0.0 | 2.4 | 2.8 | 0.7 | 1.7 | 0.3 | 0.2 | 91.4 | 0.0 | 0.0 | 0.5 | 91.4 |
| D7 | 0.0 | 0.1 | 1.2 | 1.8 | 0.1 | 0.3 | 0.0 | 0.0 | 0.1 | 0.2 | 0.0 | 95.2 | 0.8 | 0.1 | 95.2 |
| T62 | 0.0 | 1.2 | 3.3 | 1.0 | 0.0 | 0.8 | 0.6 | 0.3 | 1.2 | 0.0 | 0.0 | 0.2 | 91.0 | 0.3 | 91.0 |
| ZIL131 | 1.0 | 0.3 | 0.0 | 0.8 | 0.0 | 1.7 | 1.2 | 0.3 | 2.3 | 1.9 | 0.9 | 0.0 | 0.0 | 89.7 | 89.7 |

Note: Four T72 and two BMP2 classifiers are designed, based on, respectively, four and two realizations of the target. Horizontal labels correspond to classifiers (four for T72 and two for BMP2). Vertical labels correspond to all targets considered when testing. Note that seven examples of T72 and one for BMP2 were not used while training. Total classification performance reflected in right-most column.

of the target realizations, and tested on all three. We show results for an example choice of the four T72 and two BMP2 training selections, although we found in practice this decomposition was not critical (e.g. which four particular T72 targets were chosen was not critical, as long as they captured the variation in the physical makeup of the targets). The TRUMPETS data associates different “serial numbers” with the eleven T72 and three BMP2 targets, and these are identified in the discussion below.

In Table III we present results for a 6° aperture, using 0.1° sampling, as was considered in Table II. The classifiers for the T72 and BMP2 targets were trained as discussed above, while the classifiers for the other eight targets (each only having one serial number) were trained as in the previous results. In Table III we present results in which the horizontal identifies all classifiers (four for the T72, two for the BMP2, and one for all other targets). The vertical axis identifies all testing examples (eleven for the T72, three for the BMP2, and one for all others). The right-most column reflects “total” performance, defined as follows. For the T72 the total performance is reflective of the percentage of times one of the eleven T72 testing examples was associated (in a ML sense) with one of the four T72 classifiers. For the BMP2 the total performance is reflective of the percentage of times one of the three BMP2 testing examples was associated with one of the two BMP2 classifiers. For the remaining eight targets total performance is reflective of the likelihood that the training data is associated with the proper classifier

(there is only one source of training and testing data for these cases).

The results in Table III indicate that the target complexity, and variation between different realizations of the same target yields classification degradation. Nevertheless, the results in Table III do indicate that the algorithm generally does a reasonable job of classifying a target, even when the particular realization of the target was not seen prior to testing. The degradation in Table III underscores that the technique developed here is most appropriate for moving targets, for which a priori pose information is often available (such information was not used here, for the fixed targets in this data set).

V. CONCLUSIONS

We have addressed multiaspect target classification using a sequence of HRR waveforms. The sequence of waveforms are processed via an HMM, the states of which reflect a generally contiguous set of target-sensor orientations for which the wave scattering is relatively stationary. The sequence of HRR profiles, from a given target, implicitly samples HMM states. When performing classification, the target identity and orientation (pose) are unknown, and therefore the sequence of states being sampled is “hidden.” We have characterized the statistics of the HMM states in the context of feature parsing, with such performed via RELAX [13]. A state-dependent statistical model has been devised for the variation of the RELAX features.

The multiaspect HRR problem is highly complicated by the size of the radar wavelength

relative to characteristic target dimensions. The high degree of resolution offers potential for classification, but it also leads to scattering that changes very quickly with aspect. This has led to the large number of HMM states used in the classifiers. In the results presented here there are 120 states for each target, over a 360° azimuthal extent. One can use fewer states, but classification performance deteriorates. In future research the model must be extended to perform the state decomposition over 4π steradians, with states defined by solid angles. This will lead to a very large number of states, reflective of target complexity. However, in practice one may limit the number of states under test. For example, for HRR sensing of airborne targets, one can use Doppler processing to estimate the target flight path. Such information can significantly reduce the number of states that must be examined when testing the HMM. This underscores our earlier observations that the method present here is most appropriate for moving targets.

APPENDIX A

The ML estimate of the HMM parameters λ is formulated as

$$\lambda_{\text{ML}} = \arg \max[\log P(O | \lambda)] \quad (17)$$

where recall that $O = \{o_1, o_2, \dots, o_M\}$ is the sequence of M observations. The motivation of the EM algorithm is that associated with the observation data O there can be some unobservable or hidden data such that if the hidden data were made known it would be easier to fit the observed data to the model [16]. In our case the states are hidden. The key to the EM algorithm is to devise an auxiliary function [16]

$$Q(\bar{\lambda} | \lambda) = E_{Q|O, \lambda} \log P(O, Q | \bar{\lambda}) \quad (18)$$

where Q is the hidden data, O is the observed data, λ and $\bar{\lambda}$ are the present and new parameters, respectively.

The EM algorithm consists of the following two steps [16]: step 1 (expectation) in which we compute $Q(\bar{\lambda} | \lambda^k) = E_{Q|O, \lambda^k} \log P(O, Q | \bar{\lambda})$, and step 2 (maximization) in which we find $\lambda^{k+1} = \arg \max_{\bar{\lambda}} Q(\bar{\lambda} | \lambda^k)$. It can be shown that λ^k will increase monotonically to a maxima [16], although not necessarily to a global maxima.

We now apply the EM algorithm to the HRR-HMM and derive the extended Buam–Welch algorithm. For training $O = \{o_1, o_2, \dots, o_M\}$ there exist a set of possible states paths, with invalid paths accounted for by the paths with one or more zero probability transitions. Denote a state path as $Q =$

$\{q_1, q_2, \dots, q_M\}$, then

$$\begin{aligned} & \log P(O, Q | \bar{\lambda}) \\ &= \log \left[\bar{\pi}_{q_1} P(o_1 | q_1, \bar{\lambda}) \prod_{m=1}^{M-1} \bar{a}_{q_m q_{m+1}} P(o_{m+1} | q_{m+1}, \bar{\lambda}) \right] \\ &= \log \bar{\pi}_{q_1} + \log P(o_1 | q_1, \bar{\lambda}) \\ & \quad + \sum_{m=1}^{M-1} [\log \bar{a}_{q_m q_{m+1}} + \log P(o_{m+1} | q_{m+1}, \bar{\lambda})]. \end{aligned} \quad (19)$$

Taking conditional expectation $E_{Q|O, \lambda}$ of (19) and using the Markov property of Q , we have

$$\begin{aligned} Q(\bar{\lambda} | \lambda) &= E_{Q|O, \lambda} [\log \bar{\pi}_{q_1} + \log P(o_1 | q_1, \bar{\lambda})] \\ & \quad + \sum_{m=1}^{M-1} E_{Q|O, \lambda} [\log \bar{a}_{q_m q_{m+1}} + \log P(o_{m+1} | q_{m+1}, \bar{\lambda})] \\ &= \sum_{n=1}^N P(q_1 = s_n | O, \lambda) [\log \bar{\pi}_n + \log P(o_1 | q_1 = s_n, \bar{\lambda})] \\ & \quad + \sum_{m=1}^{M-1} \left[\sum_{i=1}^N \sum_{j=1}^N P(q_m = s_i, q_{m+1} = s_j | O, \lambda) \log \bar{a}_{ij} \right. \\ & \quad \left. + \sum_{n=1}^N P(q_{m+1} = s_n | O, \lambda) \log P(o_{m+1} | q_{m+1} = s_n, \bar{\lambda}) \right] \end{aligned} \quad (20)$$

which is the expectation step. Substituting (12)–(13) into (20), we have

$$\begin{aligned} Q(\bar{\lambda} | \lambda) &= \sum_{n=1}^N \gamma_1(n) P(q_1 = s_n | O, \lambda) \\ & \quad \times [\log \bar{\pi}_n + \log P(o_1 | q_1 = s_n, \bar{\lambda})] \\ & \quad + \sum_{m=1}^{M-1} \left[\sum_{i=1}^N \sum_{j=1}^N \xi_m(i, j) \log \bar{a}_{ij} + \sum_{n=1}^N \gamma_{m+1}(n) \right. \\ & \quad \left. \times \log P(o_{m+1} | q_{m+1} = s_n, \bar{\lambda}) \right]. \end{aligned} \quad (21)$$

To accomplish the maximization step, we differentiate $Q(\lambda | \bar{\lambda})$ with respect to each parameter and equate the result to zero.

For the state transition matrix \mathbf{A} and initial state distribution π , we must preserve the constraints $\sum_{j=1}^N a_{ij} = 1$ and $\sum_{j=1}^N \pi_j = 1$. These constraints are implemented via Lagrange multipliers, as in a traditional HMM [14], the results from which are given in (14) and (15).

We now focus on the HMM parameters required for the RELAX-based density function in (9), this component unique to the methodology presented here. For the parameters in (9), i.e., $\lambda_G =$

$(\mathbf{a}_{c_1}, \mathbf{a}_{c_2}, \dots, \mathbf{a}_{c_N}; \mathbf{r}_{c_1}, \mathbf{r}_{c_2}, \dots, \mathbf{r}_{c_N}; \eta_1^2, \eta_2^2, \dots, \eta_N^2) \in \bar{\lambda}$, with $(\mathbf{a}_{c_n}, \mathbf{r}_{c_n})$ the RELAX features for the code associated with state n , and η_n^2 is the associated variance, we have

$$\frac{\partial Q(\bar{\lambda} | \lambda)}{\partial \bar{\lambda}_G} = \sum_{m=1}^M \sum_{n=1}^N \left[\gamma_m(n) \frac{\partial \log P(o_m | q_m = s_n, \bar{\lambda})}{\partial \bar{\lambda}_G} \right]. \quad (22)$$

From (9) we have

$$P(o_m | q_m = s_n, \bar{\lambda}) = \frac{1}{\sqrt{2\pi\bar{\eta}_n^2}} \times \exp \left[-\frac{\mathbf{a}_{o_m}^T \mathbf{W}_{o_m o_m} \mathbf{a}_{o_m} + \bar{\mathbf{a}}_{c_n}^T \bar{\mathbf{W}}_{c_n c_n} \bar{\mathbf{a}}_{c_n} - 2\mathbf{a}_{o_m}^T \bar{\mathbf{W}}_{o_m c_n} \bar{\mathbf{a}}_{c_n}}{2\bar{\eta}_n^2} \right]. \quad (23)$$

Substituting (23) into (22) yields for $\bar{\mathbf{a}}_{c_n}$

$$\frac{\partial Q(\bar{\lambda} | \lambda)}{\partial \bar{\mathbf{a}}_{c_n}} = \frac{-1}{2\bar{\eta}_n^2} \sum_{m=1}^M [\gamma_m(n)(2\bar{\mathbf{W}}_{c_n c_n} \bar{\mathbf{a}}_{c_n} - 2\bar{\mathbf{W}}_{o_m c_n}^T \mathbf{a}_{o_m})]. \quad (24)$$

Equating (24) to zero gives the reestimation formula

$$\bar{\mathbf{a}}_{c_n} = \frac{\bar{\mathbf{W}}_{c_n c_n}^{-1} \sum_{m=1}^M [\gamma_m(n) \bar{\mathbf{W}}_{o_m c_n}^T \mathbf{a}_{o_m}]}{\sum_{m=1}^M \gamma_m(n)}. \quad (25)$$

Similarly, we obtain for $\bar{\mathbf{r}}_{c_i}$

$$\begin{aligned} \frac{\partial Q(\bar{\lambda} | \lambda)}{\partial \bar{\mathbf{r}}_{c_n}} &= \sum_{m=1}^M \gamma_m(i) \bar{\mathbf{a}}_{c_n} \circ [\bar{\mathbf{W}}_{o_m c_n} (\mathbf{a}_{o_m} \circ \bar{\mathbf{r}}_{o_m}) - \bar{\mathbf{W}}_{c_n c_n}^{\text{diag} \rightarrow 0} (\bar{\mathbf{a}}_{c_n} \circ \bar{\mathbf{r}}_{c_n})] \\ &\quad - \bar{\mathbf{r}}_{c_n} \circ \left[\sum_{m=1}^M \gamma_m^{(k)}(n) \bar{\mathbf{a}}_{c_n} \circ (\bar{\mathbf{W}}_{o_m c_n} \mathbf{a}_{o_m} - \bar{\mathbf{W}}_{c_n c_n}^{\text{diag} \rightarrow 0} \bar{\mathbf{a}}_{c_n}) \right] \end{aligned} \quad (26)$$

where \circ denotes the element-wise multiplication of two vectors of the same dimension, and $\bar{\mathbf{W}}_{c_n c_n}^{\text{diag} \rightarrow 0}$ is $\bar{\mathbf{W}}_{c_n c_n}$ with the diagonal elements set to zero. Because of the nonlinear functional form of (26) with respect to $\bar{\mathbf{r}}_{c_n}$ (note $\bar{\mathbf{r}}_{c_n}$ appears in $\bar{\mathbf{W}}_{o_m c_n}$ and $\bar{\mathbf{W}}_{c_n c_n}^{\text{diag} \rightarrow 0}$), it is not possible to derive a closed-form reestimation formula for $\bar{\mathbf{r}}_{c_n}$ by setting (26) to zero. We therefore use the gradient method to accomplish the maximization of $Q(\lambda | \bar{\lambda})$ with respect to $\bar{\mathbf{r}}_{c_n}$. The re-estimation of $\bar{\mathbf{r}}_{c_n}$ is accordingly performed via the following iteration: step 1, let $\bar{\mathbf{r}}_{c_n}^{(0)} = \mathbf{r}_{c_n}$ and $k = 0$; step 2,

$$\bar{\mathbf{r}}_{c_n}^{(k+1)} = \bar{\mathbf{r}}_{c_n}^{(k)} + \rho_k \left. \frac{\partial Q(\bar{\lambda} | \lambda)}{\partial \bar{\mathbf{r}}_{c_n}} \right|_{\bar{\mathbf{r}}_{c_n} = \bar{\mathbf{r}}_{c_n}^{(k)}}, \quad k = k + 1;$$

step 3, if

$$\frac{\|\bar{\mathbf{r}}_{c_n}^{(k+1)} - \bar{\mathbf{r}}_{c_n}^{(k)}\|}{\|\bar{\mathbf{r}}_{c_n}^{(k)}\|}$$

is small enough, stop. Otherwise go to step 2. Note ρ_k in Step 2 is the learning coefficient that controls the convergence speed, and ρ_k is usually chosen as an exponentially decreasing sequence.

To obtain $\bar{\eta}_n^2$, we have

$$\begin{aligned} \frac{\partial Q(\bar{\lambda} | \lambda)}{\partial \eta_n^2} &= \sum_{m=1}^M \sum_{n=1}^N \gamma_m(n) \frac{\partial}{\partial \eta_n^2} \left[\log \frac{1}{\sqrt{2\pi\mu_n^2}} - \frac{d^2(O_m, c_n)}{2\eta_n^2} \right] \\ &= \sum_{m=1}^M \gamma_m(n) \left[-\frac{1}{2\mu_n^2} + \frac{d^2(O_m, c_n)}{2\eta_n^4} \right] \end{aligned} \quad (27)$$

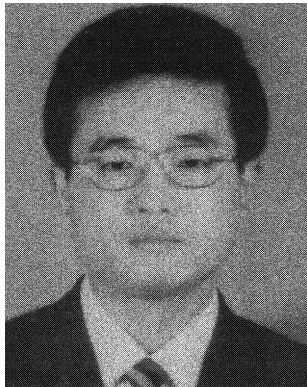
where d is the SWD as defined in (7). Equating (27) to zero, we obtain the re-estimation formula

$$\bar{\eta}_n^2 = \frac{\sum_{m=1}^M \gamma_m(n) d^2(O_m, c_n)}{\sum_{m=1}^M \gamma_m(n)}. \quad (28)$$

REFERENCES

- [1] Li, H. J., and Yang, S. H. (1993) Using range profiles as feature vectors to identify aerospace objects. *IEEE Transactions on Antennas and Propagation*, **41**, 3 (1993), 261–268.
- [2] Hudson, S., and Psaltis, D. (1993) Correlation filters for aircraft identification from radar range profiles. *IEEE Transactions on Aerospace and Electronic Systems*, **29**, 3 (1993), 741–748.
- [3] Zyweck, A., and Bogner, R. E. (1996) Radar target classification of commercial aircraft. *IEEE Transactions on Aerospace and Electronics Systems*, **32**, 2 (1996), 598–606.
- [4] Mitchell, R. A., and Westerkamp, J. J. (1999) Robust statistical feature based aircraft identification. *IEEE Transactions on Aerospace and Electronic Systems*, **35**, 3 (1999), 1077–1094.
- [5] Chiang, H.-C., Moses, R. L., and Potter, L. C. (2000) Model-based classification of radar images. *IEEE Transactions on Information Theory*, **46**, 5 (2000), 1842–1854.
- [6] Novak, L. M. (2000) State-of-the-art of SAR automatic target recognition. In *IEEE 2000 International Radar Conference Record*, 836–843.
- [7] Liao, X., Bao, Z., and Xing, M. (2000) On the aspect sensitivity of high resolution range profiles and its reduction methods. In *IEEE 2000 International Radar Conference Record*, 310–315.
- [8] Jakowatz, C. V., et al. (1996) *Spotlight-Mode Synthetic Aperture Radar: A Signal Processing Approach*. Boston: Kluwer Academic Press, Jan. 1996.
- [9] Runkle, P., Bharadwaj, P., and Carin, L. (1999) Hidden Markov model multi-aspect target classification. *IEEE Transactions on Signal Processing*, **47** (July 1999), 2035–2040.
- [10] Runkle, P., Carin, L., Couchman, L., Yoder, T. J., and Bucaro, J. A. (1999) Multi-aspect target identification with wave-based matching pursuits and continuous hidden Markov models. *IEEE Transactions on Pattern Analysis and Machine Intelligence*, **21** (Dec. 1999), 1371–1378.

- [11] Runkle, P., Nguyen, L., McClellan, J., and Carin, L. (2001) Multi-aspect target detection for SAR imagery using hidden Markov models. *IEEE Transactions on Geoscience and Remote Sensing*, **39** (Jan. 2001), 46–55.
- [12] Mitchell, R. A., and DeWall, R. (1994) Overview of high range resolution radar target identification. *Proceedings of Automatic Target Recognition Working Group*, Monterey, CA, 1994.
- [13] Li, J., and Stoica, P. (1996) Efficient mixed-spectrum estimation with application to target feature extraction. *IEEE Transactions on Signal Processing*, **44**, 2 (1996), 281–295.
- [14] Rabiner, L. R. (1989) A tutorial on hidden Markov models and selected applications in speech recognition. *Proceedings of the IEEE*, **77**, 2 (1989), 257–286.
- [15] Linde, Y., Buzo, A., and Gray, R. M. (1980) An algorithm for vector quantizer design. *IEEE Transactions on Communication*, **COM-28** (Jan. 1980), 84–95.
- [16] Moon, T. K. (1996) The expectation-maximization algorithm. *IEEE Signal Processing Magazine*, **13** (1996), 47–60.
- [17] Hawley, R. (2000) TRUMPETS development environment. Research notes, Mission Research Corporation, 2000.
- [18] O’Sullivan, J. A., DeVore, M. D., Kedia, V., and Miller, M. I. (2001) SAR ATR performance using a conditionally Gaussian model. *IEEE Transactions on Aerospace and Electronic Systems*, **37**, 1 (2001), 91–108.
- [19] Jones, III, G., and Bhanu, B. (2001) Recognizing occluded objects in SAR images. *IEEE Transactions on Aerospace and Electronic Systems*, **37**, 1 (2001), 316–328.
- [20] Fennel, M. T., and Wishner, R. P. (1998) Battlefield awareness via synergistic SAR and MTI exploitation. *IEEE Aerospace and Electronic Systems Magazine*, (Feb. 1998), 39–45.



Xuejun Liao was born in Qinghai, China. He received the B.S. and M.S. degrees in electrical engineering, from Hunan University, China, in 1990 and 1993, respectively, and the Ph.D. degree in electrical engineering from Xidian University, China, in 1999.

From 1993 to 1995, he was with the Department of Electrical Engineering, Hunan University, working on electronic instruments. From 1995 to 2000 he was with the National Key Lab for Radar Signal Processing, Xidian University, working on automatic target recognition (ATR) and radar imaging. Since May 2000, he has been working as a Research Associate with the Department of Electrical and Computer Engineering, Duke University. His current research interests are in Markovian techniques in ATR, blind methods in multichannel modeling, and information-theoretic problems in signal processing.

Paul Runkle received the B.S. degree (1998) in applied mathematics and physics from the University of Wisconsin, Madison, and the M.S. (1992) and Ph.D. (2000) degrees in electrical engineering, from the University of Michigan, Ann Arbor.

From 1993–1995 he worked at the Environmental Research Institute of Michigan on algorithm development for synthetic aperture radar and as an industrial technical consultant for the automotive industry. From 1998–2000 he served as a Research Associate in the Department of Electrical and Computer Engineering at Duke University, Durham, NC, where he developed statistical methods for multi-aspect target classification for radar and sonar. In 2001, he was a Senior Engineer with XtremeSpectrum, Inc. where he developed algorithms for ultra-wideband receiver synchronization and equalization. He joined MCNC (Microelectronics Center of North Carolina) in 2002. His current interests include system design for digital communications and statistical signal processing.

Lawrence Carin (SM’96—F’01) was born March 25, 1963 in Washington, DC and earned the B.S., M.S., and Ph.D. degrees in electrical engineering at the University of Maryland, College Park, in 1985, 1986, and 1989, respectively.

In 1989 he joined the Electrical Engineering Department at Polytechnic University (Brooklyn) as an Assistant Professor, and became an Associate Professor there in 1994. In September 1995 he joined the Electrical Engineering Department at Duke University, where he is now a Professor. Dr. Carin was the principal investigator (PI) on a Multidisciplinary University Research Initiative (MURI) on demining (1996–2001), and he is currently the PI of a MURI dedicated to multi-modal inversion.

Dr. Carin is an Associate Editor of the *IEEE Transactions on Antennas and Propagation* and a member of the Tau Beta Pi and Eta Kappa Nu honor societies. His current research interests include short-pulse scattering, subsurface sensing, and wave-based signal processing.